Probing the multi-step crystallization dynamics of micelle templated nanoparticles: structural evolution of single crystalline γ-Fe$_2$O$_3$

Kunyu Liang, Lok Shu Hui, and Ayse Turak

Department of Engineering Physics, McMaster University, Hamilton, Ontario, Canada.
Tel: (905)-525-9140 ext. 23348; E-mail: turaka@mcmaster.ca

The following supplementary details are available free of charge.

- Calculation of the single domain and paramagnetic size limits.

- Raman spectra for KBr substrate used for background subtraction.

- Selected area electron diffraction and electron energy loss spectra of iron oxide nanoparticles.

- Comparison of selected area electron diffraction, x-ray diffraction and Raman spectroscopy for iron oxide nanoparticles.

- XPS data for loaded micelles and iron oxide nanoparticles.

- Raman spectra for control experiments with solvents, precursors, and homopolymers.

- Table of expected Raman peaks for PS, HP2VP, PS-b-P2VP and o-xylene.

- Raman spectra of different loading conditions

SI1 Calculation of the single domain and paramagnetic size limits

The existence of magnetic domain walls is governed by the competition between the magnetostatic energy (E$_{MS}$), which is proportional to the particle volume (E$_{MS}$ ∼ V), and the domain wall energy(E$_{dw}$), which is proportional to the interface area of the domain (E$_{dw}$ ∼ S). When the particle size decreases beyond a certain threshold, the single domain configuration is energetically favourable. This single domain limit, related to several anisotropic energy terms, normally exists in the region from several tens to hundreds of nanometers, depending on the saturation magnetization (M$_s$).[1] The single domain critical diameter (D$_{single}$) for spherical magnetic nanoparticles could be estimated by the following equation:[2,3]

$$D_{single} \approx 36 \frac{\sqrt{AK_{eff}}}{\mu_0 M_s^2} \tag{1}$$

where A is the exchange constant, K_{eff} is the effective anisotropy constant, μ_0 is the vacuum permeability and M_s is saturation magnetization.

Below this limit, under an external magnetic field, the nanoparticle array would be magnetized such that all the magnetic moments of atoms are aligned in one direction.[4] The K_{eff} of γ-Fe$_2$O$_3$ is on the order of 4 to 8 × 10^3 J/m^3 for nanoparticles,[5,6] roughly similar to that of the bulk, while the M_s of the bulk γ-Fe$_2$O$_3$ is around 350 emu/cm^3 (note that for volume magnetization, 1emu/cm^3 converts to 10^3 A/m).[6,7] Additionally, the exchange constant is 10^{-11} J/m for γ-Fe$_2$O$_3$.[8] Therefore, one can estimate the lowest limit of D$_{single}$ for spherical γ-Fe$_2$O$_3$ nanoparticles sits at around 50nm.

The alignment of single domain nanoparticles is mostly governed by the anisotropy energy (E$_a$), which is defined as:

$$E_a = K_{eff} V \sin^2(\theta) \tag{2}$$

with V and θ representing the volume of the nanoparticles and the angle between the magnetization and the easy axis (i.e. the direction when E$_a$ is minimized).[2,9] Magnetization reversal in such particles is purely the result of magnetic moment rotation, without domain wall motion. Consequently, single domain nanoparticles could have large coercivity (H_c) compared to larger multidomain particles.[7,10]

With further decreasing size, the superparamagnetic limit would be reached at a point where the thermal energy K_BT (25.7meV) overcomes E$_a$, causing a spontaneous magnetization reversal.[3] The relaxation time for magnetization reversal is expressed by the Neel-Brown expression as follows:[2,3,11]

$$\tau = \tau_0 exp\left(\frac{K_{eff}V}{K_B T}\right) \tag{3}$$

where τ_0 is typically in the range between 10^{-11} and 10^{-9}s. Since the K_{eff} of γ-Fe$_2$O$_3$ is known,[5,6] the critical diameter that causes the spontaneous magnetization reversal can be estimated to be at around 12nm.

Below this limit, the τ shares the similar magnitude as τ_0, causing high frequency magnetization reversal, which results in zero net magnetization during a typical measurement. Hence, the nanoparticles could exhibit superparamagnetic features without H_c while maintaining a decent value of M_s. On the other hand, when the τ_m is longer than τ, the magnetization reversal cannot finish within the measurement period and thus is called the "block state".[3,12]. When $\tau_m = \tau$, the corresponding temperature is defined as the blocking temperature (T_B). According to equation 3, T_B goes down with smaller size nanoparticles, offering the ability to obtain superparamagnetism under a large temperature window.
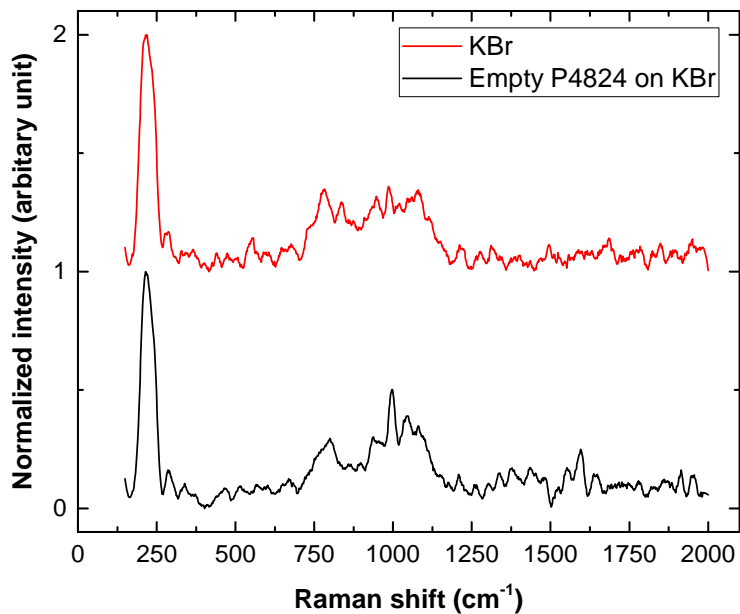
SI2   Background Kbr substraction

Figure SI1 Raman spectra of KBr for background subtraction and unsubtracted P4824 empty micelles coated KBr.

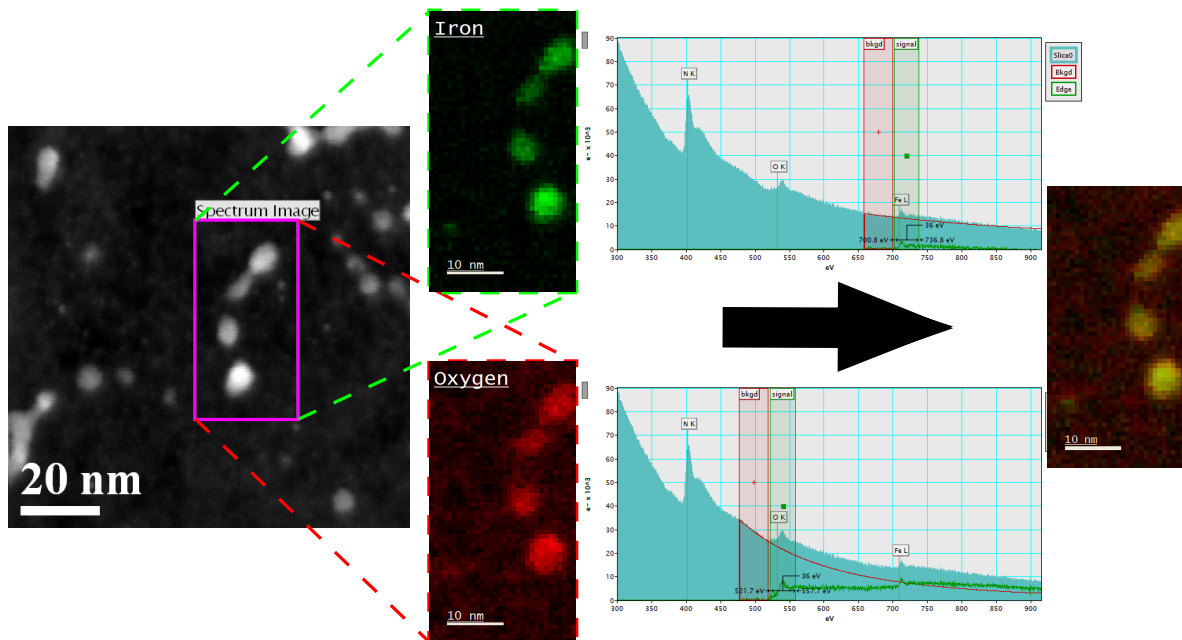## SI3   Characterization of iron oxide nanoparticles

Figure SI2 TEM micrograph of iron oxide nanoparticles with Fe and O elemental maps determined by energy selective filtering of the energy loss spectrum (EELS). Overlays of image, Fe and O maps show excellent correspondence. The loss spectra contain no features other that Fe and O from the particles, and N from the support grid. The lack of C and Cl signals suggest complete removal of the polymeric micelles and complete conversion of the $FeCl_3$
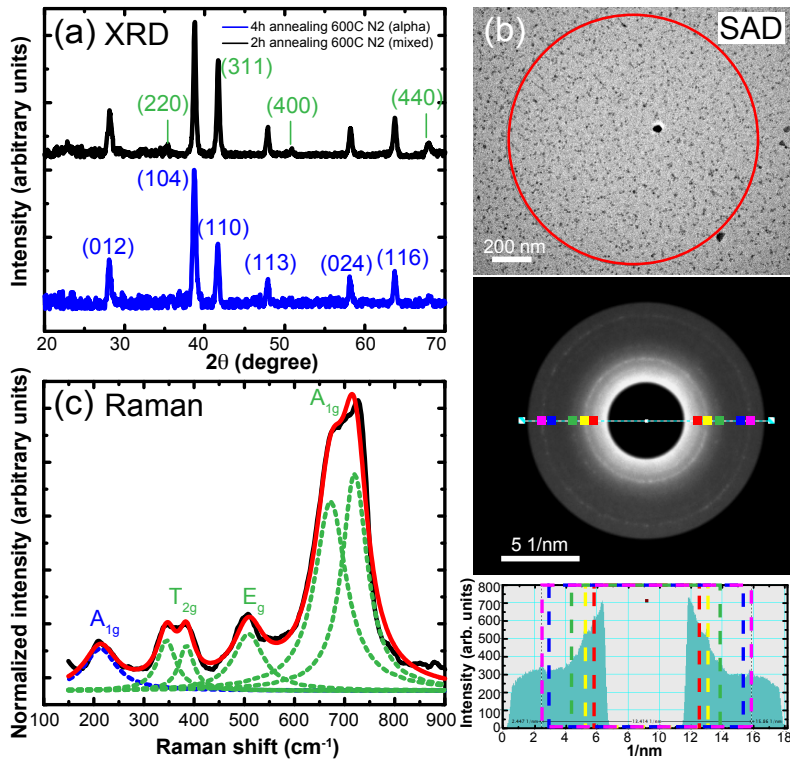
Figure SI3 Comparison of of XRD, SAD and Raman characterization for iron oxide nanoparticles after $600°$C annealing under N$_2$. (a) XRD spectrum of thick drop-cast film of nanoparticles on Si with 2h and 4h (two steps @ 2h each) annealing. Blue and green indicates crystallographic planes corresponding to α-Fe$_2$O$_3$ and γ-Fe$_2$O$_3$ phases, respectively. (b)TEM micrograph with selected area for electron diffraction, the electron diffraction pattern, and the line intensity profile of spin coated nanoparticle film with 2h annealing. Spacing observed correspond to γ-Fe$_2$O$_3$ (c) Raman spectrum of nanoparticles on KBr with 2h annealing. Blue and green indicates vibrational modes corresponding to α-Fe$_2$O$_3$ and γ-Fe$_2$O$_3$ phases, respectively.

The XPS spectra were generated by a monochromated Al Ka source (Thermo K-Alpha) with a photon energy of 1486.6 eV at a pass energy of 100.00 eV and 25.00 eV for wide range survey scans and high resolution individual core level scans. The spot size was 400 mm2. The XPS spectra was analyzed with the Thermo Avantage software tool using the Smart background correction option, which is based on the Shirley background correction method. The peaks were then fitted with Gaussian-Lorentzian functions.
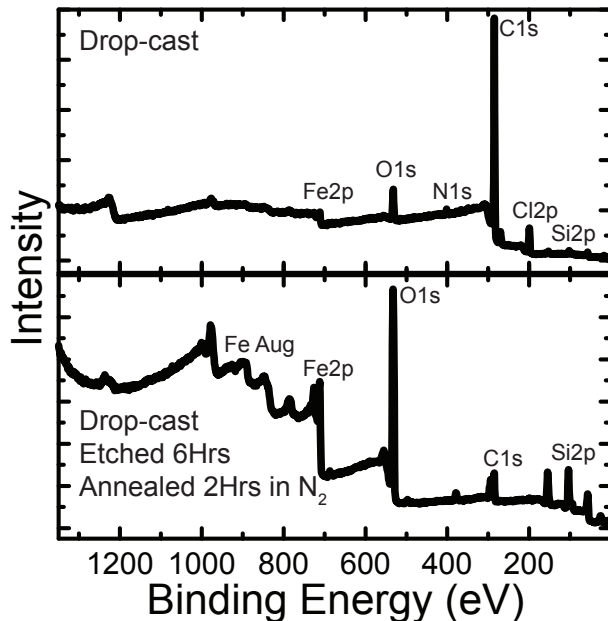

Figure SI4 XPS survey scans of thick drop-cast film of iron chloride micelles on Si (top panel) and after oxygen plasma etching for 6h and annealed at $600°$C in N$_2$ for 2h (bottom panel).

The survey spectra of a thick drop-cast film of iron chloride loaded micelles on Si and its consequential treatment by oxygen plasma etching for 6h and annealing at $600°C$ in N_2 for 2h are presented in Figure SI4. The peaks in the survey scans are identified and clearly show the removal of the polymeric micelle and evolution of the iron oxide. The most dramatic change is observed with the C1s peak due to the polymeric micelles, which decreases after treatment (though some adventitious C remains; the Cl2p, identified as chloride in the iron salt has also decreased substantially, as can be confimed from the high resolution scan in Figure SI5(a). The O1s changes substantially after the oxidation of iron chloride salt in Figure SI5(b), which can be deconvoluted into constituent components. The dominant peak (blue curve) in the O1s envelope in both scans can be attributed to water content (at 532.4eV) in the highly hygroscopic iron chloride samples,[13] as well as resulting from the native oxide of the Si substrate at 532eV. The green curve at 529.7eV in the O1s envelope corresponds to the oxide (O^{2-}), which can be assigned to Fe_3O_4[13] and Fe_2O_3 in both γ- and α- forms.[14–16] The remaining peak at 531.4eV belongs to the hydroxyl (OH^{-1}) group for which the peak position is also indistinguishable for Fe_3O_4,[13] γ- and α-Fe_2O_3.[14–16] It is therefore, difficult to infer the iron oxidation from the XPS O1s spectrum.
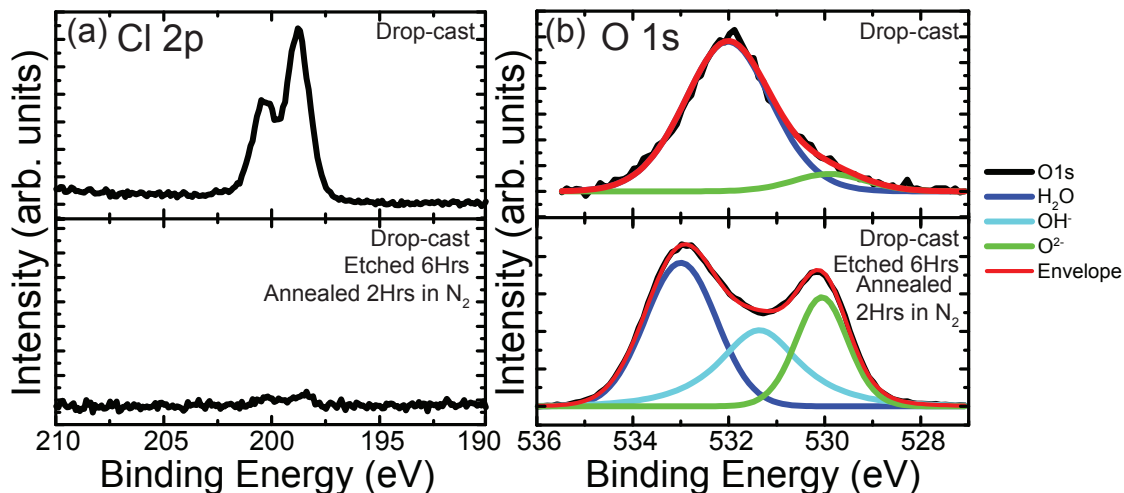

Figure SI5 XPS high resolution scans of (a) Cl2p and (b) O1s, on thick drop-cast film of iron chloride micelles on Si (top panel) and after oxygen plasma etching for 6h and annealed at $600°C$ in N_2 for 2h (bottom panel).

The high-resolution scans of Fe $2p_{3/2}$ are also shown in Figure SI6, in attempt to distinguish the form of iron oxides (bottom panel) from iron chloride (top panel). The Fe $2p_{3/2}$ envelope can be deconvoluted into several multiplets from Fe^{2+} and Fe^{3+} following the parameters provided by Grosvenor et al.[17] The multiplet splitting fits, including the pre-peak, surface peaks and saatellites,[17] are marked in Figure SI6. Grosvenor et al. demonstrated a rigorous Fe $2p_{3/2}$ peak fitting analysis of Fe_3O_4, $FeCl_3$ γ- and α- Fe_2O_3 in their work. However, they have also remarked on the similarity of peaks used to fit the envelope in all the aforesaid iron species, making an unambiguous assignment difficult.[17] From the high-resolution spectra in Figure SI6, it is possible to conclude that there may be mixed phases of iron oxides in the sample, with assignment to any of the possible iron phases. The satellite shift does suggest the formation of oxides from chlorides.
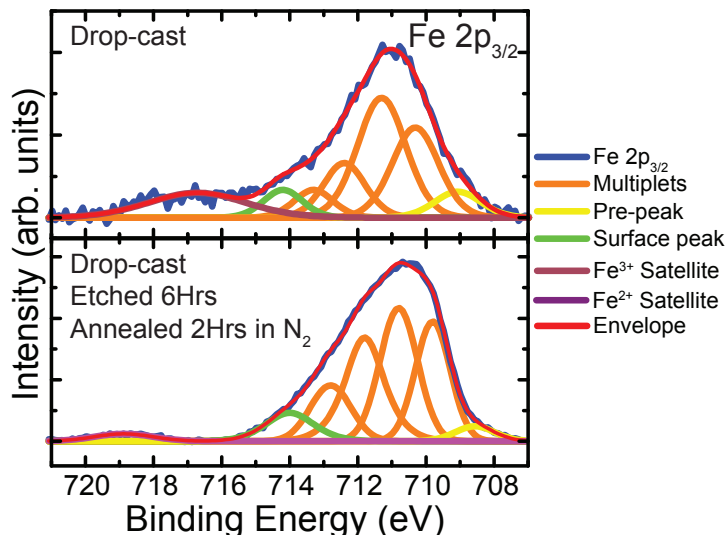

Figure SI6 XPS high resolution Fe 2p scans of thick drop-cast film of iron chloride micelles on Si (top panel) and after oxygen plasma etching for 6h and annealed at $600°C$ in N_2 for 2h (bottom panel).

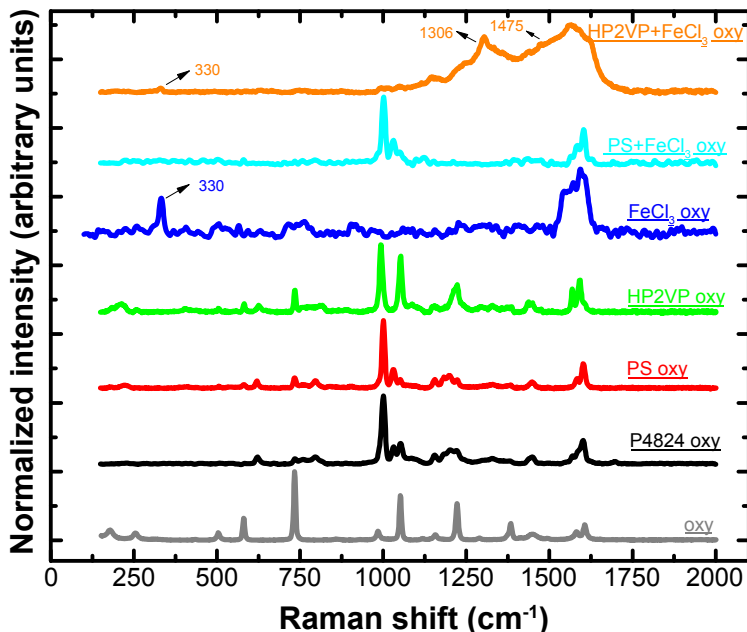## SI4   Raman spectra for control experiments

Figure SI7 Raman spectra of pristine precursors, solvent and polymers used for control experiments.

Table SI1 Table of expected Raman peaks for PS, HP2VP, PS-*b*-P2VP and o-xylene

PS [18]	HP2VP [19]	PS-*b*-P2VP [20,21]	o-xylene [22]
			585(m)
			737(vs)
	998(vs)		
1000(vs)		1000(vs)-symmetric ring breathing	
1032(m)	1056(s)	1030(m)-CH in-plane bending	1055(s)
		1050(m)-CH in-plane bending	
			1255(s)
	1572(m)	1583(m)-pyridine ring	
1585(sh)	1596(m)		1584(w)
1604(m)		1602(m)-polystyrene ring	1610(m)

*vs: very strong, s: strong, m: medium, w:weak, sh: shoulder.

SI5   Estimation of the percentage of γ-Fe$_2$O$_3$ and α-Fe$_2$O$_3$ from Raman spectra

Due to the presence of features from both the γ-Fe$_2$O$_3$ and α-Fe$_2$O$_3$ phases in the same spectrum, we used the intensity ratio of the A$_{1g}$ peak of γ-Fe$_2$O$_3$ ($\sim$ 550-800cm^{-1}) against the A$_{1g}$ of α-Fe$_2$O$_3$ ($\sim$ 150-300cm^{-1}) to make a semi-quantitative estimate of the percentage of each phase, following a modified approach similar to that by Bersani et al.[23] and Choupra et al.[24]. As Raman is more sensitive to the α-Fe$_2$O$_3$ phase, this is probably an underestimation of the amount of γ-Fe$_2$O$_3$ present in the samples. Though the Raman analysis was not correlated to the XRD data, it was used here to provide a semi-quantitative analysis of the relative abundance of each phase.

To calculate the intensity, the area of the A$_{1g}$ of the α phase and the area of the A$_{1g}$ of the γ phase were approximated using the rectangle approximation with widths of approximations as small as 2cm^{-1}.

The area intensity ratio of γ phase to α phase was given by $\Sigma = \frac{I_\gamma}{I_\alpha}$.

The percentage of γ phase to α phase was given by $\%\gamma = \frac{\Sigma}{\Sigma + 1} * 100$.

Following this approach, the $\%\gamma$ of the nanoparticles resulting from the conditions shown in Figure SI8(b) would be $\sim$90% (88%) for the micelle loaded FeCl$_3$ condition, and 0% for the unprotected FeCl$_3$ condition.

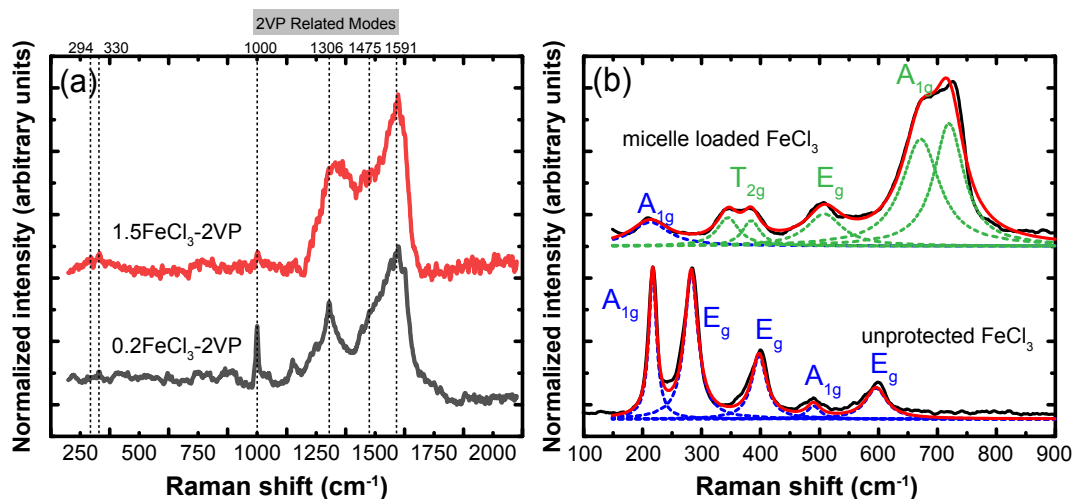## SI6   Comparison of Raman spectra for different loading conditions

Figure SI8 (a) Raman spectra of the FeCl$_3$ loaded PS-P2VP micelles with different loading ratios (b) Iron oxide nanoparticles produced with $600°$C annealing under N$_2$ for 2h with and without micelles.

References

[1] X. Batlle and A. Labarta, *J. Phys. D: Appl. Phys.*, 2002, **15**, R15–R42.

[2] A. H. Lu, E. L. Salabas and F. Schüth, *Angew. Chem., Int. Ed.*, 2007, **46**, 1222–1244.

[3] L. Wu, A. Mendoza-Garcia, Q. Li and S. Sun, *Chem. Rev.*, 2016, **116**, 10473–10512.

[4] J. Frenkel and J. Doefman, *Nature*, 1930, **126**, 274–275.

[5] D. L. Hou, X. F. Nie and H. L. Luo, *Appl Phys A*, 1998, **66**, 109–114.

[6] A. I. Figueroa, J. Bartolomé, L. M. Garćia, F. Bartolomé, A. Arauzo, A. Millán and F. Palacio, *Phys. Procedia*, 2015, **75**, 1050–1057.

[7] M. I. Dar and S. A. Shivashankar, *RSC Adv.*, 2014, **4**, 4105–4113.

[8] W. Wu, X. H. Xiao, S. F. Zhang, T. C. Peng, J. Zhou, F. Ren and C. Z. Jiang, *Nanoscale Res. Lett.*, 2010, **5**, 1474–1479.

[9] S. Laurent, D. Forge, M. Port, a. Roch, C. Robic, L. V. Elst and R. N. Muller, *Chem. Rev.*, 2008, **108**, 2064–2110.

[10] D. L. Leslie-Pelecky and R. D. Rieke, *Chem. Mater.*, 1996, **8**, 1770–1783.

[11] R. W. Chantrell, A. Lyberatos, M. El-Hilo and K. O'Grady, *J. Appl. Phys.*, 1994, **76**, 6407–6412.

[12] N. Lee and T. Hyeon, *Chem. Soc. Rev.*, 2012, **41**, 2575–2589.

[13] T. C. Lin, G. Seshadri and J. A. Kelber, *Applied Surface Science*, 1997, **119**, 83–92.

[14] A. N. Mansour and R. A. Brizzolara, *Surface Science Spectra*, 2002, **4**, 351–356.

[15] D. Barreca, E. Tondello, D. Berto, R. Gerbasi and G. A. Battiston, *Surface Science Spectra*, 2002, **8**, 240–245.

[16] S. S. Li, W. J. Li, T. J. Jiang, Z. G. Liu, X. Chen, H. P. Cong, J. H. Liu, Y. Y. Huang, L. N. Li and X. J. Huang, *Analytical Chemistry*, 2016, **88**, 906–914.

[17] A. P. Grosvenor, B. A. Kobe, M. C. Biesinger and N. S. McIntyre, *Surface and Interface Analysis*, 2004, **36**, 1564–1574.

[18] J. R. Ferraro, J. S. Ziomek and G. Mack, *Spectrochim. Acta*, 1961, **17**, 802–814.

[19] J. L. Lippert and E. S. Brandt, *Langmuir*, 1988, **4**, 127–132.

[20] W. H. Tsai, F. J. Boerio, S. J. Clarson, E. E. Parsonage and M. Tirrell, *Macromolecules*, 1991, **24**, 2538–2545.

[21] P. P. Hong, F. J. Boerio, M. Tirrell, S. Dhoot and P. Guenoun, *Macromolecules*, 1993, **26**, 3953–3959.

[22] J. Moreau and E. Rinnert, *The Analyst*, 2015, **140**, 3535–3542.

[23] D. Bersani, P. P. Lottici and A. Montenero, *J. Raman Spectrosc.*, 1999, **30**, 355–360.

[24] I. Chourpa, L. Douziech-Eyrolles, L. Ngaboni-Okassa, J.-F. Fouquenet, S. Cohen-Jonathan, M. Soucé, H. Marchais and P. Dubois, *The Analyst*, 2005, **130**, 1395.